metals

MDPI

Article

Analysis of Recrystallization Kinetics Concerning the Experimental, Computational, and Empirical Evaluation of Critical Temperatures for Static Recrystallization in Nb, Ti, and V Microalloyed Steels

Evelyn Sobotka [1,*], Johannes Kreyca [2], Robert Kahlenberg [3,4], Aurélie Jacob [1], Ernst Kozeschnik [4] and Erwin Povoden-Karadeniz [1,4]

[1] Christian Doppler Laboratory of Interfaces and Precipitation Engineering, Institute of Materials Science and Technology, TU Wien, 1060 Vienna, Austria; aurelie.jacob@tuwien.ac.at (A.J.); erwin.povoden-karadeniz@tuwien.ac.at (E.P.-K.)
[2] Voestalpine Forschungsservicegesellschaft Donawitz GmbH, 8700 Leoben, Austria; johannes.kreyca@voestalpine.com
[3] Materials Center Leoben Forschung GmbH, 8700 Leoben, Austria; robert.kahlenberg@tuwien.ac.at
[4] Institute of Materials Science and Technology, TU Wien, 1060 Vienna, Austria; ernst.kozeschnik@tuwien.ac.at
* Correspondence: evelyn.sobotka@tuwien.ac.at

Abstract: Recrystallization kinetics and two critical temperatures—the non-recrystallization temperature T_{NR} and the static recrystallization critical temperature T_{SRCT}—of five Nb, Ti, and V microalloyed steel grades are evaluated. The experimental examination is realized by employing isothermal double-hit compression tests and continuous hot torsion tests, both performed on a Gleeble® 3800 thermo-mechanical simulator. The experimental results are used for the critical assessment of predicted T_{NR} using four empirical equations from the literature, and for the validation of simulated T_{NR} and T_{SRCT}. The thermokinetic computer simulations are realized using the mean-field microstructure modeling software MatCalc. Analysis shows that higher microalloying contents increase both critical temperatures, T_{NR} and T_{SRCT}, whereby the effect of recrystallization retardation of Nb is more pronounced than that of Ti or V. The most accurate reproduction of the experimental recrystallization behavior of the five examined steel grades is realized by the employed physics-based simulation approach.

Keywords: microalloyed steel; microstructural control; precipitation; recrystallization delay; T_{NR}; T_{SRCT}; steel properties

check for updates

Citation: Sobotka, E.; Kreyca, J.; Kahlenberg, R.; Jacob, A.; Kozeschnik, E.; Povoden-Karadeniz, E. Analysis of Recrystallization Kinetics Concerning the Experimental, Computational, and Empirical Evaluation of Critical Temperatures for Static Recrystallization in Nb, Ti, and V Microalloyed Steels. *Metals* **2023**, *13*, 884. https://doi.org/10.3390/met13050884

Academic Editor: Angelo Fernando Padilha

Received: 11 April 2023
Revised: 26 April 2023
Accepted: 2 May 2023
Published: 3 May 2023

Copyright: © 2023 by the authors. Licensee MDPI, Basel, Switzerland. This article is an open access article distributed under the terms and conditions of the Creative Commons Attribution (CC BY) license (https://creativecommons.org/licenses/by/4.0/).

1. Introduction

Hot rolling processes at elevated temperatures can induce coarse and non-uniform austenite grain structures, which impair the mechanical properties of the final steel product [1,2]. Additions of microalloying elements, e.g., titanium, niobium, and vanadium, to low-carbon steel help to prevent austenite grain coarsening due to pinning of grain boundaries by precipitates and solute drag [3–5]. During thermo-mechanical treatments, the deformation-affected nucleation of (Nb/Ti/V)(C,N) MX (M standing for metallic elements, and X for C,N) carbonitride precipitates retards static recrystallization of the austenite phase and helps to control the austenite grain size [6,7]. Therefore, the formation of these complex MX particles can suppress austenite grain recrystallization in microalloyed steels. For precise planning of industrial rolling schedules at reduced costs, predictive knowledge of the temperature at which the impediment of recrystallization takes place in different microalloyed steels is crucial. The literature on the recrystallization behavior of microalloyed steel is generally based on examinations by performing isothermal double-hit compression

tests (DHT) and continuous hot torsion tests (TT) [8,9]. To date, it is in question whether one is superior to the other.

Within this work, the recrystallization kinetics of five microalloyed steel grades are examined experimentally and computationally. First, the differences and complexity of the two experimental methods, DHT and TT, for the assessment of the critical temperatures of the static recrystallization of microalloyed steel, are evaluated and discussed. These are the non-recrystallization temperature T_{NR}, Section 1.1, and the static recrystallization critical temperature T_{SRCT}, Section 1.2, respectively. Secondly, T_{NR} and T_{SRCT} values are simulated by employing the semi-physical recrystallization modeling by Buken et al. [10], which has been implemented into the mean-field microstructure modeling software MatCalc [11], http://matcalc.at (accessed on 10 April 2023). Aside from the dislocation density evolution, the thermokinetic simulation takes into account Calphad-modeled MX stabilities [12]. Thirdly, the predictive power of semi-physical simulation results on the recrystallization retardation of five experimentally studied microalloyed steel grades is compared to the purely phenomenological approach, by application of Equations (1)–(4), Section 1.1.3. The inaccuracies of these empirical equations from literature are identified and discussed.

1.1. Non-Recrystallization Temperature

The softening behavior of microalloyed steels at deformation up to ~0.5 critical strain is regulated by pure static recrystallization, whereas above it can be affected by metadynamic recrystallization. The value of the critical strain depends on microalloying, the strain rate, and temperature [13,14]. In the majority of microalloyed steels, dynamic recrystallization of the austenite matrix does not occur below an equivalent strain of 0.35, even at elevated temperatures [15].

The non-recrystallization temperature (T_{NR}) is the temperature, below which complete static recrystallisation between consecutive rolling passes does no longer occur. T_{NR} is determined for continuous cooling [16]. It is notable that T_{NR} thus also depends on the inter-rolling pass time.

1.1.1. The Role of Process Parameters for T_{NR}

The value of T_{NR} is strongly dependent on process parameters during thermo-mechanical treatments. Significantly prolonged intermediate holding times between passes, increasing strain rates, higher strains, and lower cooling rates lead to a decrease in T_{NR} [17–19]. The condition of the austenite matrix before the deformation also plays a vital role in the T_{NR}, since increasing reheating temperatures elevate the non-recrystallization temperature due to higher austenite supersaturation concerning microalloying elements [20]. Deformation below T_{NR} results in elongated austenite grains, where so-called 'pancaking' occurs due to accumulated strain, and more nucleation sites for grain boundary ferrite are provided [16,17]. At conventional controlled rolling, roughing passes are performed above T_{NR} to ensure complete recrystallization of the austenite grains during the interpass time [21].

1.1.2. The Impact of Microalloying Elements on T_{NR}

Extensive literature is available on the role of the alloying elements Nb, Ti, and V on the T_{NR} [16,19,22,23]. Higher amounts of microalloying elements lead to an increase in the non-recrystallization temperature. Figure 1 shows the comparison of different microalloying and associated T_{NR}. Additions of Nb increase the T_{NR} more effectively than those of V and Ti [24,25]. Akben et al. [26] reported that both Nb carbonitrides and dissolved Nb in the steel matrix have a higher impact on recrystallization retardation than solute V. Abad et al. [20] differentiate between deformation at low and high pass-strains (φ) within their experiments using Nb-microalloyed steel. They show that at $\varphi = 0.1$, recrystallization is impeded by solute drag due to dissolved Nb, while strain-induced precipitation is the controlling factor at $\varphi > 0.2$.

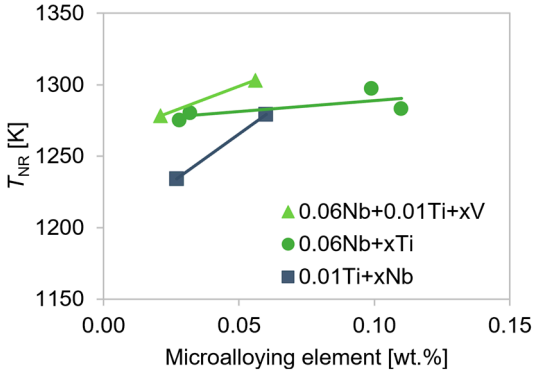

Figure 1. Impact of varying contents (x) of microalloying elements on T_{NR} of microalloyed steels for deformation to φ = 0.2 and intermediate holding time of 5 s [25,27]. Lines are guides to the eye.

(Nb/Ti/V)(C,N) precipitates possess the ability to elevate T_{NR}, but increasing the interpass time causes coarsening of the carbonitrides [27]. At first, prolonged holding elevates the T_{NR}, since pinning by deformation-induced carbonitrides increases. A prolongation of the interpass time above 50 s, on the other hand, reduces their power for recrystallization impediment [27] due to coarsening of the precipitates, which leads to a decrease in T_{NR}. Besides the substantial effect of grain boundary pinning by deformation-induced particles, further physical mechanisms, such as solute drag of microalloying elements, affect T_{NR} [17,20]. According to Bai et al. [17], solute drag dominates at short interpass times below 12 s within their research on microalloyed steel.

1.1.3. Empirical Equations for T_{NR}

An empirical relation between the increase in T_{NR}, induced by the microalloying elements Nb, Ti, and V, was given for low-carbon steels by Boratto et al. [28] with

$$T_{NR} = 887 + 464\mathrm{C} + 890\mathrm{Ti} + \left(6445\mathrm{Nb} - 644\sqrt{\mathrm{Nb}}\right) + \left(732\mathrm{V} - 230\sqrt{\mathrm{V}}\right) + 363Al - 357Si, \quad (1)$$

where the chemical composition is to be entered in wt.% [29].

Unfortunately, the content of nitrogen, which is essential for the formation of (Nb/Ti/V)(C,N) precipitates, is not taken into account.

Homsher [25,27] presented an equation for T_{NR} developed by Bai et al. [30]:

$$T_{NR} = 174 \log\left[\mathrm{Nb}\cdot\left(\mathrm{C} + \frac{12}{14}\mathrm{N}\right)\right] + 1444. \quad (2)$$

The variables Nb and C represent the element content of the steel grade in wt.%. N describes the amount of remaining free nitrogen after the precipitation of TiN. Therefore, the equation directly takes the effect of Nb into account and indirectly includes the impact of Ti on recrystallization via the N content.

Fletcher [31] investigated the T_{NR} values of several different steel grades, which delivered the following equation [25,27]:

$$T_{NR} = 849 - 349\mathrm{C} + 676\sqrt{\mathrm{Nb}} + 337\mathrm{V}. \quad (3)$$

Here, the microalloying elements Nb and V are accounted for in wt.%. Titanium is not mentioned.

Another equation discussed by Homsher [25,27] for the prediction of T_{NR} by Fletcher [31] is given as:

$$T_{NR} = 203 - 310\mathrm{C} - 149\sqrt{\mathrm{V}} + 657\sqrt{\mathrm{Nb}} + 683e^{-0.36\cdot\varphi}. \quad (4)$$

The content of Nb and V is given in wt.%, while φ describes the applied pass strain.

1.2. Static Recrystallization Critical Temperature

In microalloyed steel, the maximum temperature, at which the static austenite recrystallization starts to be impeded *solely* by the strain-induced precipitation of MX carbonitride precipitates, is defined as the static recrystallisation critical temperature (T_{SRCT}). It is always determined by isothermal conditions and does not involve a dependence of inter-rolling pass time. Below T_{SRCT}, no complete recrystallization of the austenite phase can thus be realized, independently of intermediate holding times during processing [18].

Figure 2 depicts the correlation between the amount of microalloying and the T_{SRCT}, as well as the applied strain, found in the literature by Medina et al. [19,23,32–35]. Higher microalloying contents of the elements Nb, Ti, and V and lower true strain values increase the T_{SRCT}. Nb has the biggest effect on recrystallization retardation, followed by V and Ti.

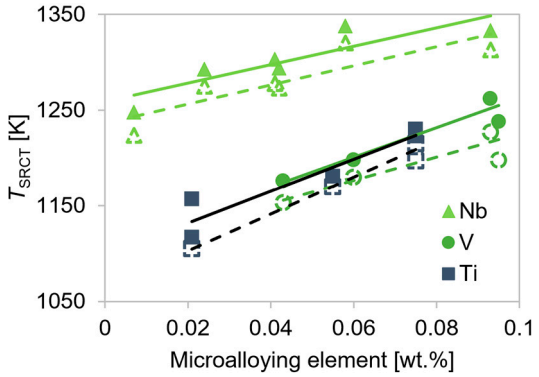

Figure 2. T_{SRCT} of microalloyed steels for deformation to φ = 0.2 (continuous line) and φ = 0.35 (dashed line) [19,23,32–35]. Lines are guides to the eye.

1.3. Comparison of T_{NR} and T_{SRCT}

Figure 3 displays experimental T_{NR} and T_{SRCT} values of Nb microalloyed steels from the literature [16,19,22,33–35]. It shows that the non-recrystallization temperature reaches lower values compared to the T_{SRCT} at longer interpass times, independently of microalloying.

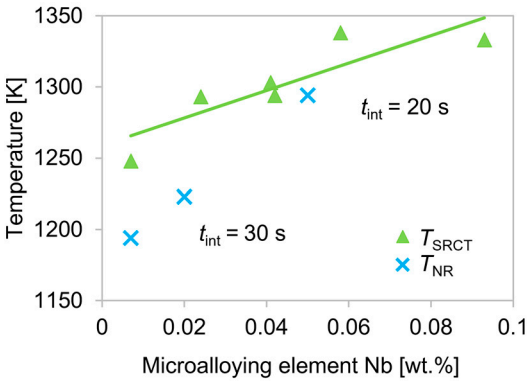

Figure 3. T_{SRCT} and T_{NR} of Nb microalloyed steels for deformation to φ = 0.2 and varying intermediate holding times [16,19,22,33–35]. The line is a guide to the eye.

Both critical temperatures indicate the start of recrystallization impediment but may deviate from each other as the T_{SRCT} only considers the recrystallization-retarding effect of precipitated carbonitrides, while the T_{NR} marks the temperature at which total static recrystallization does not occur.

2. Materials and Methods

Five different microalloyed steel grades are examined within the framework of this study. The chemical composition of the investigated alloys is given in Table 1.

Table 1. Chemical composition of examined materials in wt.%.

Steel Grade	C	Mn	Ti	Nb	V	Cr	Al	Si
S1	0.15	1.27	0.01	0.01	0.07	0.20	0.03	0.22
S2	0.18	0.88	<0.01	<0.01	<0.01	0.02	0.03	0.26
S3	0.20	1.40	<0.01	<0.01	0.10	0.02	0.02	0.30
S4	0.18	0.93	<0.01	0.03	<0.01	0.03	0.03	0.26
S5	0.21	1.45	<0.01	0.04	0.10	0.03	0.03	0.50

The microalloyed steel grade S1 contains considerable amounts of Nb, Ti, and V, but much more Cr than all other alloys. The steel grade S2 serves as reference material since it only contains low additions of Ti, Nb, and V. S3–S5 are typical microalloyed steel grades with varying contents of Nb, Ti, and V. S5 combines the effects of all three microalloying elements, while S3 and S4 just contain higher amounts of V or Nb, respectively.

2.1. Experiments

2.1.1. Double-Hit Compression Tests (DHT)

DHT are a very successful method for the determination of recrystallization kinetics in the austenite region of steels [19,23,32–35]. In fact, the softening fraction due to recrystallization is measured by this kind of experiment. By the examination of the softening fraction (all phase fractions in the present study are given in mol.%) of austenite at different temperatures and varying holding times before the second deformation, the T_{NR} and T_{SRCT} can be determined.

Double-hit tests are performed on a Gleeble® 3800 thermo-mechanical simulator. To ensure the comparability between the experimental test results from DHT and torsion tests, the same steel grade, S5, is investigated with both methods. On the cylindrical samples with 10 mm diameter and 15 mm length, an R-type thermocouple is welded onto the surface for temperature control during resistive heating. A layer of Mo, nickel paste, and graphite is placed between specimen and anvil to decrease the temperature gradient to < 10 K. Figure 4 depicts the schematic rolling pattern of the performed tests. The individual specimens are solution annealed at 1553 K for 600 s. Previous MatCalc equilibrium calculations by the authors [36] showed that the annealing temperature of 1553 K is above the solubility limit of MX carbonitride solid solutions, while the test temperatures (1373–1273 K) are low enough for their precipitation. After cooling down to the respective test temperature, the samples are held for 20 s and subsequently deformed to $\varphi = 0.2$ with 0.5 s^{-1}. The low strain of 0.2 is chosen to exclude dynamic recrystallization during the treatment. The first compression is followed by an intermediate holding time of 0.3–3000 s before the start of the second deformation with a strain rate of again 0.5 s^{-1} to $\varphi = 0.4$ in total.

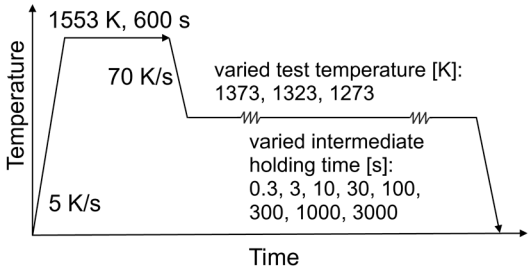

Figure 4. Thermo-mechanical rolling pattern for DHT.

For the evaluation of the softening fraction, the 5% true strain method [37] is applied. Using this technique, the fraction of the recrystallized material can be identified when no significant recovery contributions are expected [38], and the softening fraction of the material is here calculated by the following equation: [37]

$$X_a = \frac{\sigma_{m(5\%)} - \sigma_{2(5\%)}}{\sigma_{m(5\%)} - \sigma_{1(5\%)}}, \quad (5)$$

where $\sigma_{m(5\%)}$ is the true stress in the zero-softening curve at 5% strain. The zero softening curve describes the deformation and, therefore, the evolution of the true stress up to the maximum true strain of 0.4, without an intermediate holding time or an interruption for a second hit, while the parameters $\sigma_{1(5\%)}$ and $\sigma_{2(5\%)}$ describe the flow stresses at 5% strain for the first and the second deformation, respectively. Since the holding between the deformation hits initiates recrystallization of the material, the second flow curve would be identical to the first one after a sufficiently long intermediate holding due to complete recrystallization [21]. In the work of Homsher [25], the accurate identification of the different stress values is illustrated and discussed in detail.

For the evaluation of the T_{NR} from DHT, the fractional softening of the material is plotted as a function of the different deformation temperatures [39]. The corresponding value of T_{NR} is determined at 20% fractional softening, since earlier studies showed that below 20 percent, softening is caused by static recovery, whereas, above this limit, it is evoked by static recrystallization [25,27,39].

By plotting the fractional softening as a function of time, the T_{SRCT} can be evaluated. At the T_{SRCT}, as well as below this temperature, the slope of X_a against time decreases [19]. A plateau is formed at lower temperatures, which indicates the deformation-induced precipitation of MX particles [25] and the retardation of recrystallization. Above the T_{SRCT}, no impediment of recrystallization due to precipitation of (Nb/Ti/V)(C,N) takes place.

2.1.2. Hot Torsion Tests (TT)

Hot torsion tests with continuous cooling are performed on all five steel grades using the hot torsion mobile conversion unit of the Gleeble® 3800 thermo-mechanical simulator. The experimental setup is similar to the one of the DHT but torsion tests demand for a more complex sample shape with 165 mm length, a diameter of 10 mm at the center, and a diameter of 14 mm at the borders. The specimens for the experiments are solution annealed at 1553 K for 600 s, followed by constant cooling from 1553 K with 1 K/s. During cooling, the samples undergo deformation consisting of 15 passes with 0.3 equivalent strain and a strain rate of 2 s^{-1}. The strain of 0.3 is not sufficient to produce dynamic recrystallization; therefore, the examination of static recrystallization can be focused on. The interpass time between the individual torsional loads is 30 s. The schematic rolling pattern for the torsion tests is illustrated in Figure 5.

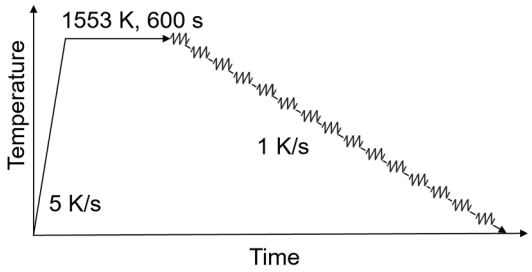

Figure 5. Thermo-mechanical rolling pattern for continuous hot torsion tests.

The experimentally obtained values of torque T and twist θ provide the basis for the calculation of the effective stress σ_{eff} and strain φ_{eff} according to the von Mises criterion, adapted from Maccagno and Medina et al. [15,29]:

$$\sigma_{\text{eff}} = \frac{\text{T} \cdot 3.3\sqrt{3}}{2\pi R^3}, \tag{6}$$

$$\varphi_{\text{eff}} = \frac{\theta R}{\sqrt{3}L}, \tag{7}$$

where the value of 3.3 accounts for strain rate sensitivity as well as strain hardening of the examined microalloyed steels [40], R is the radius, and L represents the length of the individual sample. The mean flow stress (*MFS*) corresponds to the area under each stress–strain ($\sigma - \varphi$) curve of the separate passes, normalized by the applied strain, and can be calculated by the following equation: [17,29]

$$MFS = \frac{1}{\varphi_{\text{b}} - \varphi_{\text{a}}} \int_{\varphi_{\text{a}}}^{\varphi_{\text{b}}} \sigma_{\text{eq}} d\varphi_{\text{eq}}. \tag{8}$$

By use of the *MFS* plotted against the inverse absolute temperature during the deformation, T_{NR} is identified by a change in the slope of the curve [17,41].

For the examination of the T_{SRCT} from torsion tests, isothermal torsion experiments at varied temperatures with the same strain and strain rate are necessary. The T_{SRCT} can then be evaluated from the plot of fractional softening against time and it is, therefore, independent of the interpass time [18,19].

3. Modeling

3.1. Substructure and Recrystallization Model

The MatCalc simulations in the present work utilize the modeling framework for static recrystallization implemented by Buken et al. [10], which incorporates the combined influence of nucleation, growth and coarsening of recrystallized grains based on the dislocation density evolution and precipitation kinetics [42]. The relevant equations, as implemented in MatCalc (version 6.04.0087), are summarized in the subsequent sections.

3.1.1. Dislocation Density Evolution

The substructure is described with an extended one-parameter dislocation density evolution model based on the work of Kocks and Mecking [43]. The three terms control the generation of dislocations (A), dynamic recovery (B), and static recovery (C) [36]:

$$\frac{\partial \rho}{\partial \varphi} = \frac{M}{b\boldsymbol{A}}\sqrt{\rho} - 2\boldsymbol{B}M\frac{d_{\text{crit}}}{b}\rho - 2\boldsymbol{C}D_{\text{eff}}\frac{Gb^3}{\dot{\varphi}kT}\left(\rho^2 - \rho_{\text{eq}}^2\right), \tag{9}$$

where ρ describes the total dislocation density, ρ_{eq} the dislocation density of a well-annealed microstructure, φ the true strain, M the Taylor factor, b the Burgers vector, d_{crit} the critical annihilation distance between two dislocations [10], D_{eff} the effective diffusion coefficient, G the shear modulus, $\dot{\varphi}$ the strain rate, k the Boltzmann constant, and T the temperature. The effective diffusion coefficient used in this work accounts for pipe diffusion due to dislocations D_{Dis}, according to the work by Stechauner and Kozeschnik [44].

The parameter ρ_{eq} is obtained from the sum of the equilibrium value for internal dislocations $\rho_{\text{eq,int}}$ and the Read–Shockley dislocation density required to uphold the given subgrain structure ρ_{RS} [10,45]:

$$\rho_{\text{eq}} = \rho_{\text{eq,int}} + \rho_{\text{RS}}. \tag{10}$$

The effect of precipitates on dislocation generation is not taken into account.

3.1.2. Grain Boundary Pinning and Solute Drag

Carbonitride precipitates as well as alloying elements in solid solution both hinder grain boundary movement via Zener pinning [46] and solute drag [47], respectively. The implementation in MatCalc treats both effects within the mobility calculations. The effective mobility M_{eff} for simultaneous precipitation and solute drag is combined in the same way for high angle grain boundaries (HAGBs) and low angle grain boundaries (LAGBs): [48]

$$\frac{1}{M_{\text{eff}}} = \frac{1}{M_{\text{prec}}} + \frac{1}{M_{\text{sol}}}. \tag{11}$$

In a system with precipitates, the intrinsic grain boundary mobility is reduced to M_{prec}, depending on the driving pressure for grain boundary movement and the Zener pressure [48]. The mobility term M_{sol} accounts for the solute drag of elements according to Cahn's model [47].

3.1.3. Nucleation of Recrystallized Grains

According to the theory developed by Bailey and Hirsch [49], subgrains that are in contact with high angle grain boundaries may evolve into recrystallized grains, provided that the subgrain diameter δ exceeds a critical value δ_{crit}, which is calculated as [10]:

$$\delta_{\text{crit}} = \frac{4 \cdot \gamma_{\text{HAGB}}}{P_{\text{D,RX}}} = \frac{4 \cdot \gamma_{\text{HAGB}}}{0.5Gb^2\left(\rho_{\text{tot}} - \rho_{\text{eq,int}}\right)}, \tag{12}$$

where γ_{HAGB} is the high angle grain boundary energy and $P_{\text{D,RX}}$ is the driving pressure for recrystallization. The nucleation rate of new grains $\dot{N}$ depends on the number density of potential nucleation sites N_{pot}, the flow of subgrains reaching the critical size $\dot{F}$ (as determined by the time evolution of the subgrain distribution) and the saturation function B, which accounts for the fraction of HAGBs occupied by recrystallized nuclei. Thus, the consumption of nucleation sites is

$$\dot{N} = N_{\text{pot}} \cdot \dot{F} \cdot B. \tag{13}$$

A more detailed summary of the calculation procedure for the nucleation rate can be found in [10].

3.2. Simulation Setup

Both the T_{NR} and the T_{SRCT} are affected by the intricate interplay between the deformation impact, MX carbonitride precipitation, and recrystallization behavior of the austenite matrix. MatCalc simulations of the thermo-mechanical treatments are performed to describe the deformation-dependent dislocation density evolution, the precipitation kinetics, and the progress of recrystallization. The models (see Section 3.1) are finally calibrated with the experimentally determined softening fractions, the T_{SRCT}, and the T_{NR} of the examined steel grades.

In Table 2, the input variables used for the dislocation density evolution as well as the recrystallization and coarsening of the five microalloyed steel grades are summarized.

Table 2. Parameter symbols and values for thermokinetic MatCalc simulations.

Symbol	Name	Value	Unit	Source
α	Strengthening coefficient	0.12	-	[36]
ν	Poisson's ratio	0.30	-	MatCalc default value
G	Shear modulus	$\frac{193{,}000-73.33\cdot T[^\circ C]}{2(1+\nu)}$	MPa	MatCalc default value
b	Burgers vector	2.50×10^{-10}	m	MatCalc default value
M	Taylor factor	3.06	-	MatCalc default value
k	Boltzmann constant	1.381×10^{-23}	JK^{-1}	MatCalc default value
D_{eff}	Effective diffusion coefficient	$6.4x\ 10^{-2} \exp\left(-\frac{119{,}000}{RT}\right)$	m^2s^{-1}	MatCalc default value
D_{GB}	Grain boundary diffusion coeff.	$7.9x\ 10^{-1} \exp\left(-\frac{141{,}000}{RT}\right)$	m^2s^{-1}	MatCalc default value
D_{CB}	Cross-boundary diffusion coeff.	$2{\cdot}D_{\text{B}}$	m^2s^{-1}	[50]
$\rho_{\text{eq,int}}$	Internal equilibrium dislocation density	10^{11}	m^{-2}	MatCalc default value
γ_{HAGB}	HAGB-energy	0.5	Jm^{-3}	[51]
γ_{LAGB}	LAGB-energy	0.3	Jm^{-3}	MatCalc default value
ω	Grain boundary width	1×10^{-9}	m	[50]
$\eta_{\text{HAGB,int}}$	Free HAGB-prefactor	0.015	-	[48]
$\eta_{\text{LAGB,int}}$	Free LAGB-prefactor	10	-	MatCalc default value
$\eta_{\text{HAGB,pin}}$	Pinned HAGB-prefactor	0.001	-	This work
$\eta_{\text{LAGB,pin}}$	Pinned LAGB-prefactor	0.001	-	This work
k_{d}	Pre-factor for coarsening	2	-	This work
$E_{\text{B,Ti}}$	Binding energy of Ti	10,000	$Jmol^{-1}$	[48]
$E_{\text{B,Nb}}$	Binding energy of Nb	11,000	$Jmol^{-1}$	This work
$E_{\text{B,V}}$	Binding energy of V	3000	$Jmol^{-1}$	This work
$T_{\text{crit,MX}}$	Highest possible solution temperature of (Nb/Ti/V)(C,N) *	3073/4073/2543	K	This work
λ	Mixing coefficient	$(1 - X_{\text{av}})^2$	-	MatCalc default value

* Determined from equilibrium peak temperature of the miscibility gap of respective Fe-MX systems.

Note that, in the precipitation and recrystallization simulation setup, instead of considering the full mixing/demixing of solute atoms Ti, Nb, and V with C and N, the mixing between the substitutional microalloying atoms is assumed to be negligible. This goes along with microanalysis of MX particles, which shows clear separation between Ti-rich, Nb-rich, and V-rich types in comparable steel grades [52–54]. Three separate MX compounds, Nb(C,N), Ti(C,N), and V(C,N), are used, accordingly, which was for the benefit of the numerical stability during the thermokinetic simulations.

Previous research by the authors [36] revealed that the dislocation density evolution (Equation (9)) for microalloyed steel can be reasonably well approximated by using the temperature- and strain rate-dependent parameters A, B, and C, depicted in Figure 6.

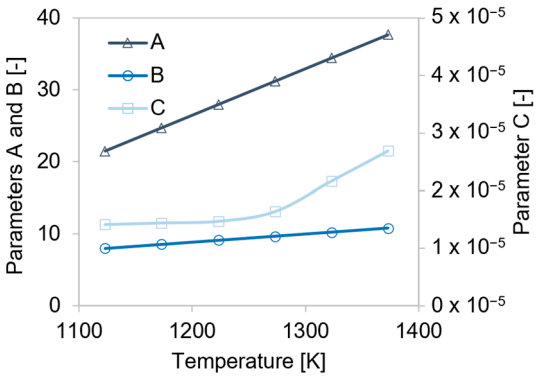

Figure 6. ABC parameters used for isothermal compression tests with strain rate of 0.5 s^{-1}. Lines are guides to the eye.

4. Results and Discussion

4.1. Experiments

Our research has shown that torsion tests are less time-consuming, given that only one specimen and a single thermo-mechanical treatment is needed for the evaluation of the T_{NR} for a specific material. At double-hit tests, a high number of experiments and extensive data analysis are necessary to examine the recrystallization behavior at different temperatures and varying holding times for the assessment of a corresponding T_{NR} and T_{SRCT}. When comparing the information about the recrystallization behavior received by the two different experimental methods, DHT are somewhat superior as the entire recrystallization evolution between two deformations is represented and both critical temperatures can be evaluated.

4.1.1. Double-Hit Compression Tests

Figure 7 depicts the flow curves of alloy S5 from DHT at three different test temperatures and varying holding times before the second deformation. The critical strain, which divides stress–strain curves in static and metadynamic recrystallization is not reached yet, as it is strongly related to the unattained maximum stress of the curve [14]. Therefore, pure static recrystallization is observed.

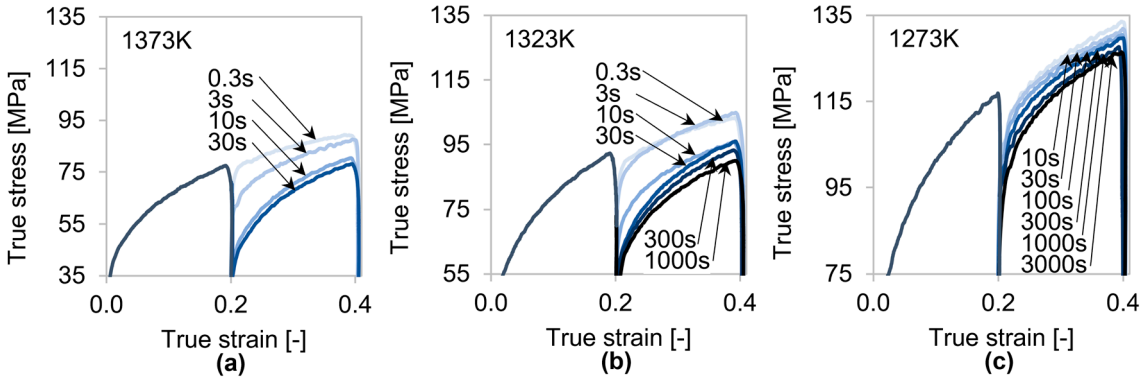

Figure 7. Flow curves of steel grade S5 during isothermal DHT with varying deformation temperatures and intermediate holding times. (**a**) 1373 K, 0.5 s^{-1}, 0.3–30 s; (**b**) 1323 K, 0.5 s^{-1}, 0.3–1000 s; (**c**) 1273 K, 0.5 s^{-1}, 10–3000 s.

At higher temperatures, lower true stress values are generally attained. A reduction in the intermediate holding time between the two hits increases the yield stress of the second hit. Since shorter holding times after the first hit induce static recrystallization, work hardening becomes more pronounced at the second deformation. Additionally, the grain refinement due to the recrystallization is concomitant with the formation of new grain boundaries, which impede the deformation of the material and result in higher stress peaks at the second hit.

The softening fraction is derived by applying the 5% true strain method on the experimentally determined flow curves, Figure 8a. The non-recrystallization temperature for DHT with a 30 s interpass time is determined at 1274 K. An increase in the intermediate holding time shifts the T_{NR} to lower temperatures.

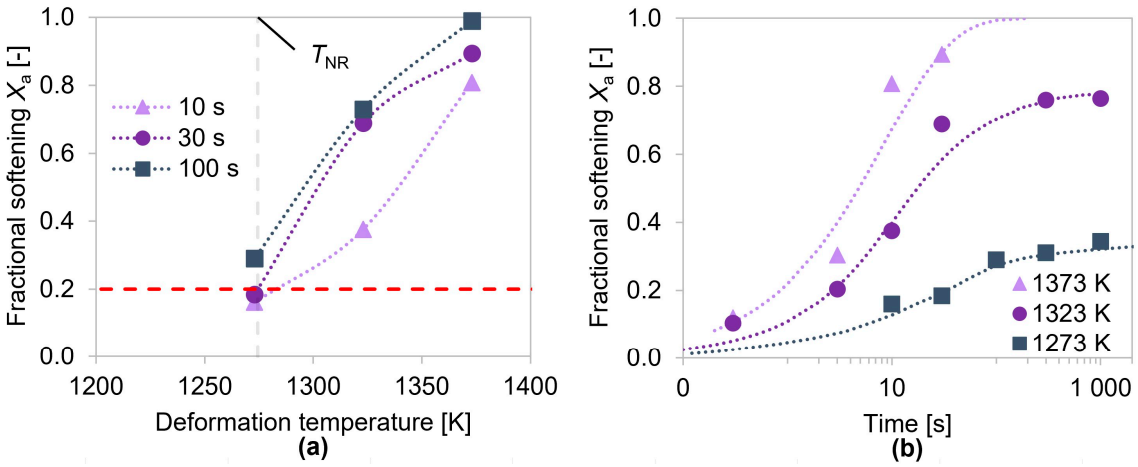

Figure 8. Evaluated T_{NR} of steel grade S5 from isothermal DHT with 0.5 s^{-1} strain rate and 30 s interpass time (**a**); effect of deformation temperatures 1373–1273 K on softening fractions of steel grade S5 derived from isothermal double-hit compression tests with 0.5 s^{-1} strain rate (**b**). Dotted lines are guides to the eye.

In Figure 8b, the influence of the test temperature on the softening of alloy S5 is illustrated. As a result of higher grain boundary mobilities at elevated temperatures, the softening fraction increases. At 1373 K, the material is fully recrystallized after approximately 100 s and the sigmoidal graph equals those of steels without microalloying. Retardation of recrystallization due to the strain-induced formation of MX can be observed at temperatures $\leq$ 1323 K. As a consequence, the T_{SRCT} of alloy S5 is defined as 1323 K, the temperature, where the formation of (Nb/Ti/V)(C,N) precipitates starts. Thus, recrystallization is impeded, and the slope of the softening fraction against time is decreased. This effect becomes stronger at the lower deformation temperature of 1273 K, indicative from Figure 8b.

4.1.2. Hot Torsion Tests

The resulting stress–strain curve of alloy S1 during the continuous torsion experiment clearly shows that the effective stress rises at a higher effective strain and decreasing temperature (Figure 9a). Figure 9b–f display the derived mean flow stresses as a function of the inverse temperatures for all materials. The T_{NR} values are identified by the intersection point of a vertical auxiliary line—which indicates the onset of the slope change in the flow curve—with the *x*-axis [41]. The experimental T_{NR} of alloy S2 is determined at 1156 K, representing the lowest value of all studied materials. This is in line with the fact that S2 contains the lowest amount of microalloying elements. The higher non-recrystallization temperatures of the other alloys can be explained by the deformation-induced precipitation of Ti-, Nb-, and V-carbonitrides, which impede the recrystallization. When comparing S3 and S4, it is evident that the high Nb content in S4 leads to strongly retarded recrystallization, whereas alloy S3, with high V contents and smaller amounts of Nb, exhibits lower T_{NR} values. The recrystallization impediment due to V(C,N) is less pronounced compared to Ti- or Nb-carbonitrides.

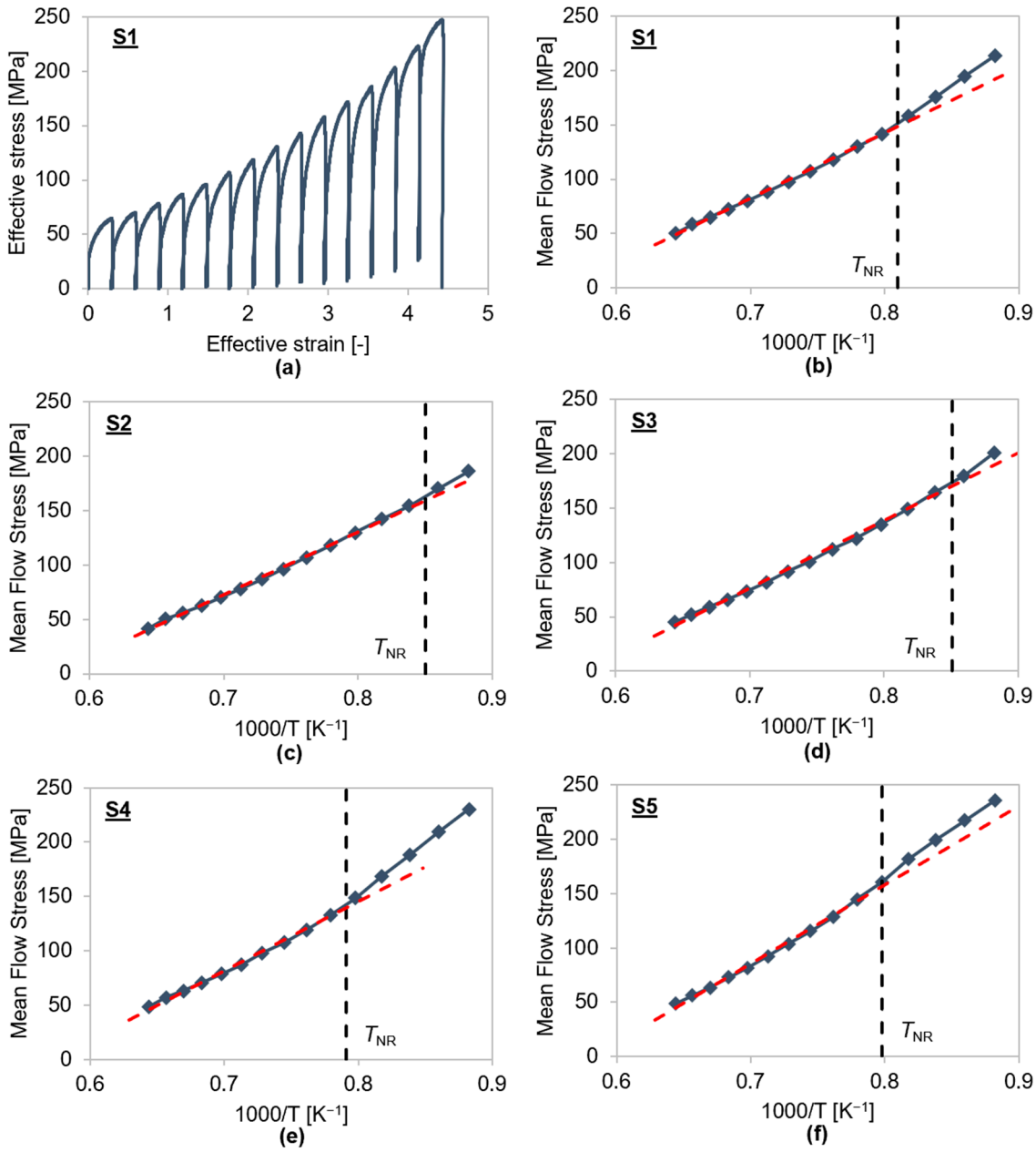

Figure 9. Stress–strain curves of steel grade S1 (**a**) and dependence of MFS on inverse absolute temperature for steel grades S1–S5 corresponding to a 15-pass torsion sequence (**b**–**f**). Lines are guides to the eye.

The slope change in the mean flow stress curves in Figure 9 allows the graph to be divided into two zones. The first region refers to the deformation at elevated temperatures and the *MFS* increases as the temperature drops. In this zone, complete recrystallization of the austenite phase takes place between each pass and recrystallization-controlled rolling is achieved. Since the microstructure fully recrystallizes, no work hardening caused by dislocations remains in the final microstructure. The stress increase is solely induced by the increasing yield strength at lower temperatures. The second region is defined as deformation below T_{NR}, where hardly any recrystallization occurs between the passes and the stress increases due to the accumulation of dislocations in the austenite phase from pass to pass. Figure 9 also shows that, with increasing *MFS*, the tendency for strain hardening also increases.

4.2. Simulation

Isothermal single-hit compression tests on the basis of the temperature profiles given in the schematic schedule of Figure 4 with a strain rate of 0.5 s^{-1} up to a total strain of 0.2 are simulated for all five investigated steel grades. Subsequently, prolonged holding at the respective test temperature is added to examine the time-dependent evolution of austenite recrystallization after the single-hit deformation.

Figure 10 illustrates the simulated softening fraction of the five alloys plotted against the deformation temperatures. T_{NR} of the examined materials is determined by the intersection point of the corresponding curve and the auxiliary line for 20% fractional softening.

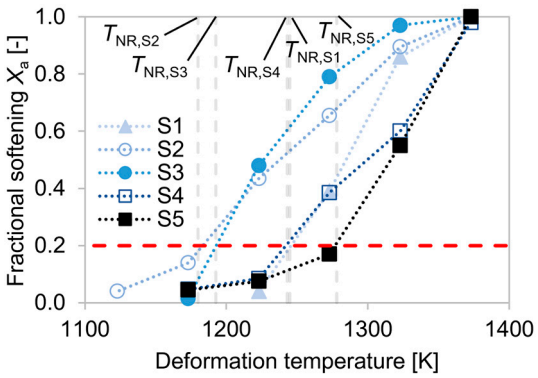

Figure 10. Determination of T_{NR} from simulated isothermal compression tests with 0.5 s^{-1} strain rate to 0.2 strain for alloys S1–S5. Dotted lines are guides to the eye.

The lowest value of T_{NR} is determined for the reference alloy S2, which contains negligible amounts of microalloying elements. The non-recrystallization temperatures of the other steel grades rise in the sequence S3 (highest V and high Ti), S4 (high Ti and Nb), S1 (highest Ti and Cr; high Nb, V), and S5 (highest Nb, V; high Ti).

Figure 11 depicts the temperature-dependent softening fractions of the materials S1–S5 as a function of holding times after deformation. The slopes of the graphs clearly change at the respective static recrystallization critical temperatures and a plateau is formed due to deformation-induced precipitation of MX particles. As the retarding pressure decreases at prolonged holding times due to precipitate coarsening, the curves continue afterwards with a sigmoidal shape.

The simulation results show that larger amounts of microalloying result in higher values of the T_{SRCT}. In the alloy S2, which does not contain significant amounts of Ti, Nb, and V, the inhibition of recrystallization is triggered only below 1173 K. S1 and S3 reach the T_{SRCT} at 1223 K, as both alloys contain a sufficient amount of V to impede recrystallization at a higher temperature. Contrary to the Ti-, Nb-, and V-microalloyed S5, the material S4 only contains Nb, which explains why the T_{SRCT} of the material is located at a lower temperature of 1273 K. The simulated static recrystallization temperature of S5 is in close agreement with the experiments, as both methods result in a high T_{SRCT} of 1323 K.

Figure 12 depicts the simulated time–temperature–precipitation (TTP) curves without deformation for 5% precipitated relative phase fraction of (Nb/Ti/V)(C,N) MX compounds for the investigated steel grades. During simulation of the single-hit compression tests, MX phases form right at the minimum start temperature for precipitation, T_{PS}, of the corresponding TTP curve. A decrease in temperature accelerates the nucleation of new carbonitride phases until T_N, which describes the temperature at the "nose" of the TTP curve, is reached. Above T_N, precipitation is strongly impeded by low driving forces, even though diffusion would be high. The opposite is true at temperatures below T_N. Thus, at a temperature of ~973 K, significant precipitation does not occur within a technologically relevant holding time (expectedly below 10 h).

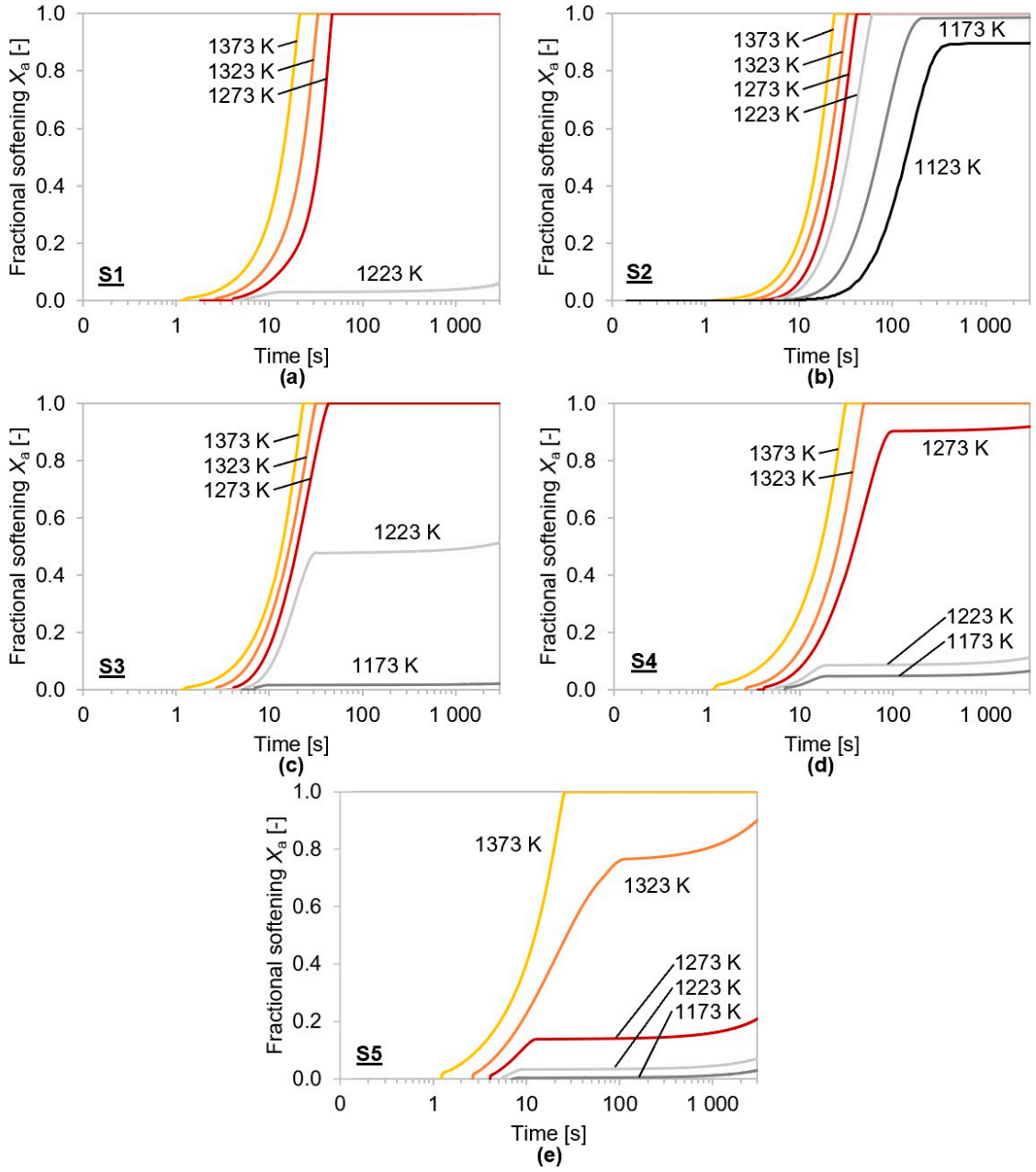

Figure 11. Effect of deformation temperatures on softening fractions of steel grades S1–S5, (**a**–**e**), derived from simulated isothermal compression tests with 0.5 s^{-1} strain rate up to 0.2 strain.

In Figure 13, the T_{PS} and T_N of the individual MX phases from simulated TTP curves and the T_{NR} from simulated compression tests are compared to the experimental T_{NR} from hot torsion tests. The evaluated non-recrystallization temperatures are in the range of T_N, where the peak of microalloy carbonitride precipitation is located. This indicates sound simulative thermokinetics of MX precipitation, since it is expected that the impediment of recrystallization is governed by grain boundary pinning by MX phases [5]. Due to the low solubility of Ti(C,N) in austenite, this phase is observed at higher temperatures than Nb(C,N) and V(C,N) [36]. Thus, microalloying of titanium is highly effective for grain boundary pinning by individual MX phases at elevated temperatures. Only in alloy S4 does the formation of Nb(C,N) start at a higher temperature than Ti(C,N) due to the much lower content of Ti in comparison to Nb.

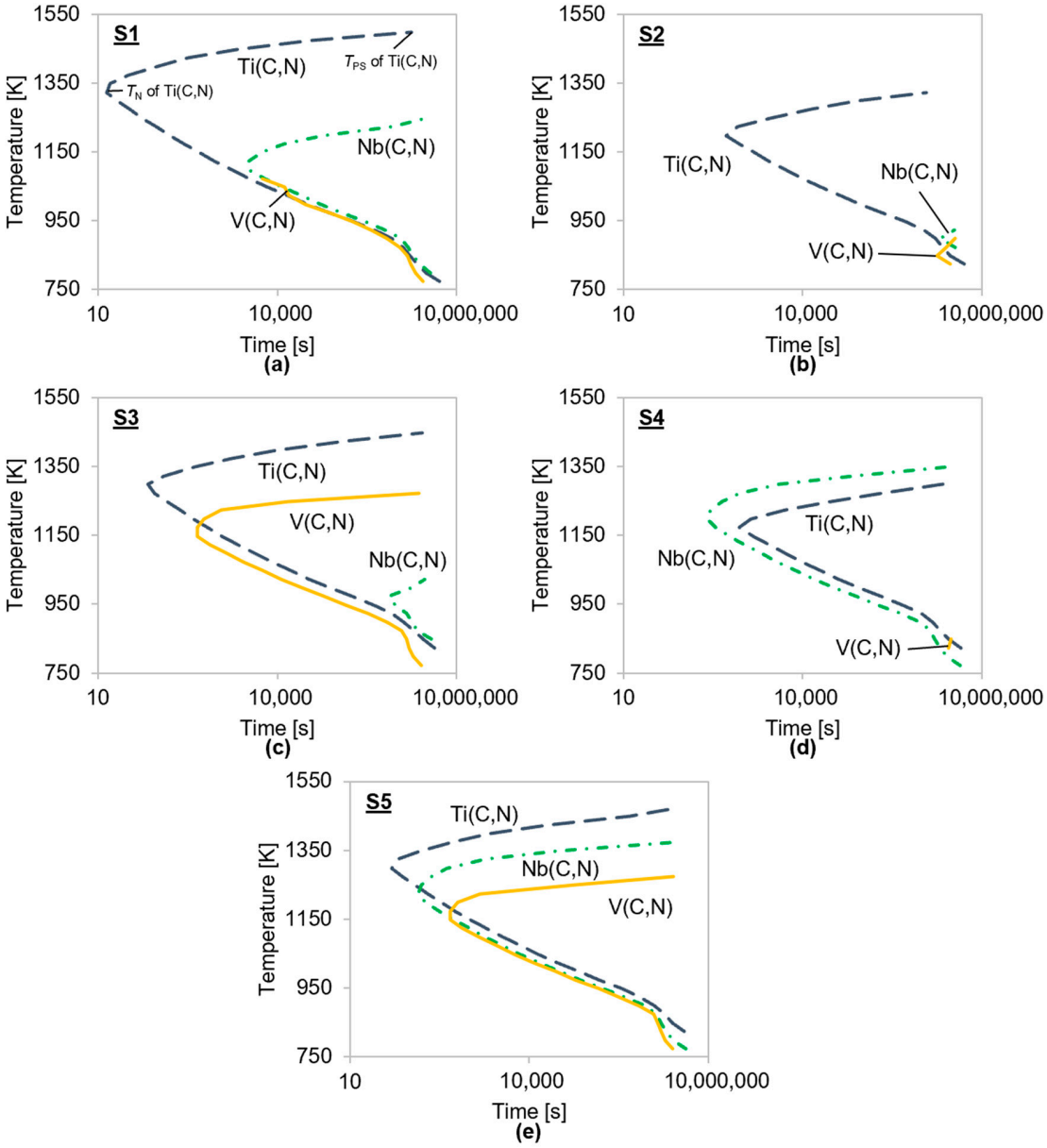

Figure 12. Computed TTP curves for 5% precipitated fraction of individual MX phases for alloys S1–S5, (**a**–**e**).

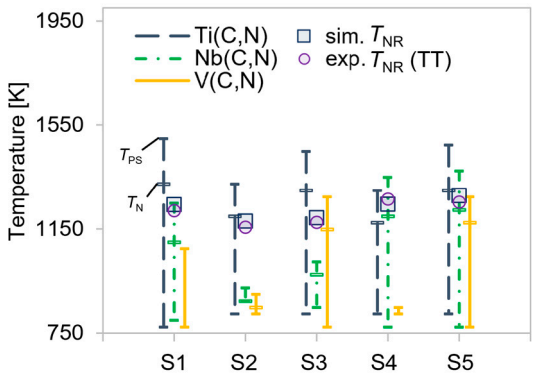

Figure 13. Comparison of T_{PS} and T_N from simulated TTP curves and T_{NR} from simulated compression tests with 0.5 s^{-1} strain rate up to 0.2 strain to experimental T_{NR} from hot torsion tests for alloys S1–S5.

The impeding influence on the static recrystallization is explained by the combination of austenite grain boundary pinning of precipitates and solute drag of the substitutional elements Nb, Ti, and V. To examine which of these two mechanisms predominates during the recrystallization retardation, the formation of (Nb/Ti/V)(C,N) phases and the remaining dissolved elements, causing solute drag in the matrix during deformation, are examined in detail. Figure 14 presents the atomic fractions of the microalloying elements Nb, Ti, and V in the austenite matrix and the softening fraction of austenite during the simulation of the compression tests at the determined non-recrystallization temperature of each steel grade.

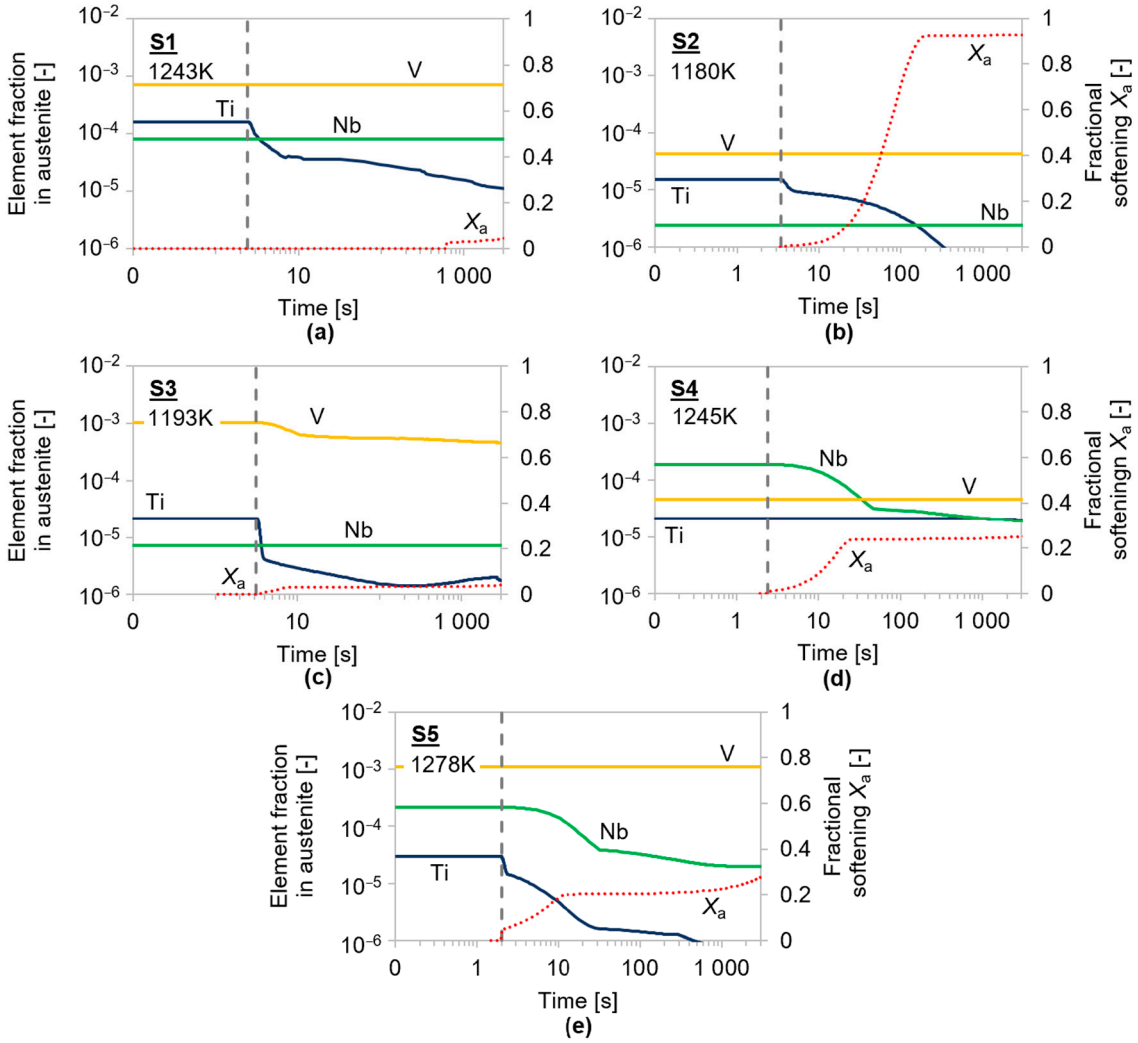

Figure 14. Atomic fraction of microalloying elements in austenite (continuous lines) and softening fraction of austenite (dotted lines) during compression tests at respective simulated T_{NR} of the alloy S1–S5, (**a**–**e**). The vertical dashed lines indicate the start of deformation with 0.5 s^{-1} strain rate to 0.2 strain.

The softening fraction clearly increases at the beginning of the deformation. The simultaneous strain-induced precipitation of carbonitrides, as seen by the drop of the respective dissolved element fraction, hinders the grain boundary movement subsequently. After compression start, significant amounts of dissolved microalloying elements in austenite are observed in the alloys S1, S3, S4 and S5. Here, a combination of precipitate pinning and solute drag is likely relevant for the retarded static recrystallization. In S2, due to the low microalloying content, no significant effect of either precipitation and solute drag is observed, and recrystallization is, thus, fastest.

Nevertheless, the effect of solute drag is expected to be presumably small, since the amount of precipitated carbonitrides is assumed to be sufficient for the present retardation of recrystallization. The results correlate well with the literature; Abad et al. [20] reported that solute drag only has a high impact on recrystallization at a small strain $\varphi = 0.1$.

4.3. Comparison of Experimental and Predicted T_{NR} and T_{SRCT}

Figure 15 summarizes the results of the experimentally derived critical temperatures for static recrystallization from double-hit tests (exp. T_{SRCT} (DHT), exp. T_{NR} (DHT)) and torsion tests (exp. T_{NR} (TT)) as well as the corresponding temperatures resulting from recrystallization simulation (sim. T_{SRCT}, sim. T_{NR}). The T_{SRCT} from compression tests of S5 matches exactly with the simulated value and the experimental T_{NR} also correlates well with the simulated one. Medina et al. [23] stated that T_{NR} and T_{SRCT} overlap in experiments with the same experimental setup. Our obtained results confirm this, since the experimental and simulation-based T_{SRCT} show only minor deviations from the determined T_{NR} values. For the alloys S3, S4, and S5, the value of the simulated T_{NR} is $\leq$ 45 K lower than that of the simulated T_{SRCT}, while the T_{NR} of S1 and S2 slightly exceed the T_{SRCT} ($\leq$20 K). This difference in the trend may be explained by the quite large temperature step of 50 K for the test temperatures, used within the simulations for the determination of T_{SRCT}. A smaller temperature step within the simulation increases the T_{SRCT} of S1 and S2 above the computational T_{NR}. Furthermore, the simulation results confirm that higher microalloying contents increase both critical temperatures. The alloy S2, with the lowest T_{SRCT} and T_{NR}, contains hardly any microalloying additions, while the alloy S5, with the highest contents of Nb, Ti, and V, reaches the highest values of T_{SRCT} and T_{NR}.

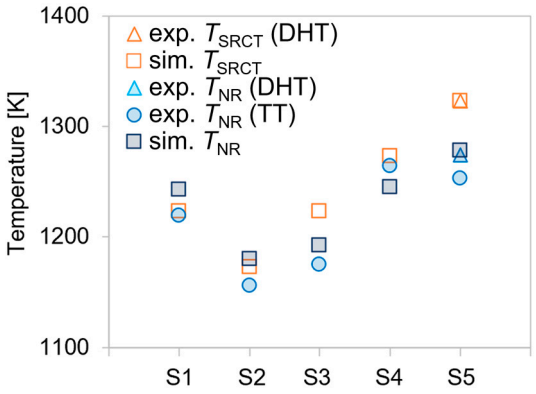

Figure 15. Comparison of experimentally determined recrystallization critical temperatures to values from semi-physical recrystallization simulation for alloys S1–S5.

Figure 16 compares the T_{NR} values calculated with Equations (1)–(4) and the simulation results to the experimental values from torsion tests. The physics-based simulation of the present study matches the experimental data best, followed by the empiric relation of Boratto et al. [28], which shows a systematic relatively small underestimation of about 50 K.

This is in contrast to the findings by Homsher [25,27], who claimed that the obtained values from the Boratto equation would exceed their experimental ones. It is notable that Homsher's alloys contain twice as much Nb (~0.06 wt.%) as the steel grades of the present study. Since Equation (1) attributes a large impact on the T_{NR} to Nb, it may only be applied for alloys with lower Nb content. Equation (2) by Bai et al. [30], on the other hand, coincides with the experimental data of Homsher (max. C content of 0.062 wt.%) but shows the highest deviation for our experiments. Only alloy S1, which contains the lowest amount of C (0.15 wt.%), shows a negligible difference between the experimental T_{NR} and the value derived from Equation (2). This indicates that the equation by Bai should only be applied to steels with very low C levels. Equations (3) and (4) by Fletcher [25,27] match the trend in our experimental data, but the T_{NR} values are roughly 60 K and 120 K too low, respectively. Both equations exclude the impact of N and Ti, which are known to elevate T_{NR} during

recrystallization. The consideration of the applied strain in Equation (4) does not raise the values to the predicted temperatures. These comparisons clearly show the problem of empiric relations. Whereas each of the empiric equations may precisely match experimental data in a narrow composition range without any relation to processing parameters, their predictive power is limited.

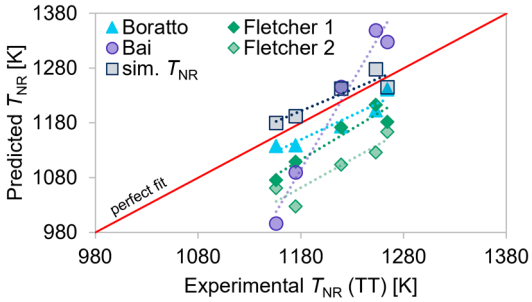

Figure 16. Comparison of experimentally determined T_{NR} from torsion tests and simulation to values calculated from empirical equations for alloys S1–S5. The red line indicates zero deviation between predicted and experimental T_{NR}. Dotted lines are guides to the eye.

5. Conclusions

Good consistency between the two experimental methods, isothermal double-hit compression tests (T_{NR} and T_{SRCT}) and continuous hot torsion tests (T_{NR}), for the determination of the critical temperatures for static recrystallization of five microalloyed steel grades is achieved in our work. Concerning the information about recrystallization kinetics, investigations using double-hit experiments should be preferred as they allow us to study the interpass time, and both critical temperatures can be determined from the same experimental setup. The main disadvantage of double-hit compression tests is the large number of tests needed for the determination of T_{NR} and T_{SRCT}. Torsion testing is less time-consuming as it only demands one sample to obtain T_{NR}, but the applied experimental procedure does not cover the investigation of T_{SRCT}.

The moderate interpass time of 30 s in DHT initiates deformation-supported precipitation of MX phases, which leads to grain boundary pinning and retardation of recrystallization. The effect of solute drag is negligible in our experiments with a strain of 0.2 per hit.

The experimental data for the T_{NR} and the T_{SRCT} are compared to a semi-physical parameter-based simulation model for static recrystallization in combination with a mean-field dislocation density evolution model. Our investigations lead to a maximum deviation of the simulation results for T_{NR} by less than 50 K from the experimental data throughout the investigated microalloying contents. A benefit of our simulation approach, aside from its high predictive power, is that we additionally obtain predictions on the T_{SRCT}. The according simulation results are consistent with experimental data, exemplarily determined for S5 with the highest microalloying contents of the studied steel grades.

The comparative computations with T_{NR} values are calculated by using four empirical equations from the literature, showing that most of the proposed empirical formulae deviate from the experimental data, indicated by a difference between evaluated and experimental T_{NR} of more than 100 K. The equations do not take processing parameters into account and can only be employed for a narrow composition range. Only the formula by Boratto et al. yields a more appropriate trend for T_{NR} with varying microalloying, with a systematic deviation around 50 K.

To conclude, the critical temperatures for static recrystallization T_{NR} and T_{SRCT} are significantly raised by the microalloying element Nb, rather than Ti and V. The best match of all experimental data of the studied steel grades is obtained by the simulation with combined thermodynamic and microstructural semi-physical modeling. The physical-based predictions additionally help to understand the interplay of steel compositions and precipitation kinetics with recrystallization. Nevertheless, there are limitations concerning

the applied parameters and models as metadynamic or dynamic recrystallization are not taken into account. The ABC parameters for the dislocation density evolution are evaluated for the current process parameters and have to be adapted to the temperature and strain rate. It can be stated that the recrystallization behavior of the examined microalloyed steel grades during the performed treatments can be thoroughly simulated by computational mean-field microstructure modeling, and it therefore helps to reduce the extent of preliminary experimental investigations for future industrial process optimizations. The developed and validated semi-physical modeling approach has high predictive power for T_{NR} and T_{SRCT} for wide composition variations within microalloyed steel.

Author Contributions: Conceptualization, E.S., J.K. and E.P.-K.; methodology, E.S.; software, E.S.; investigation, E.S.; writing—original draft preparation, E.S. and R.K.; writing—review and editing, E.S., J.K., A.J., E.K. and E.P.-K.; visualization, E.S.; supervision, E.P.-K. All authors have read and agreed to the published version of the manuscript.

Funding: This research was funded by Christian Doppler Forschungsgesellschaft in the framework of the CD-Laboratory of Interfaces and Precipitation Engineering (CDL-IPE).

Institutional Review Board Statement: Not applicable.

Informed Consent Statement: Not applicable.

Data Availability Statement: Not applicable.

Acknowledgments: The financial support from the Austrian Federal Ministry for Digital and Economic Affairs and the National Foundation for Research, Technology, and Development is gratefully acknowledged. The authors acknowledge Open Access Funding by TU Wien. The financial support, as well as the provision of sample material by voestalpine Tubulars GmbH & Co. KG, is gratefully acknowledged by the authors.

Conflicts of Interest: The authors declare no conflict of interest. The funders had no role in the design of the study; in the collection, analyses, or interpretation of data; in the writing of the manuscript; or in the decision to publish the results.

References

1. Liu, Z.G.; Gao, X.H.; Xiong, M.; Li, P.; Misra, R.; Rao, D.Y.; Wang, Y.C. Role of hot rolling procedure and solution treatment process on microstructure, strength and cryogenic toughness of high manganese austenitic steel. *Mater. Sci. Eng. A* **2021**, *807*, 140881. [CrossRef]
2. Sauer, M.; Fabík, R.; Schindler, I.; Kawulok, P.; Opěla, P.; Kawulok, R.; Vodárek, V.; Rusz, S. Analysis of the microstructure development of Nb-microalloyed steel during rolling on a heavy-section mill. *Materials* **2022**, *16*, 288. [CrossRef]
3. Varanasi, R.S.; Gault, B.; Ponge, D. Effect of Nb micro-alloying on austenite nucleation and growth in a medium manganese steel during intercritical annealing. *Acta Mater.* **2022**, *229*, 117786. [CrossRef]
4. Stornelli, G.; Tselikova, A.; Mirabile Gattia, D.; Mortello, M.; Schmidt, R.; Sgambetterra, M.; Testani, C.; Zucca, G.; Di Schino, A. Influence of vanadium micro-alloying on the microstructure of structural high strength steels welded joints. *Materials* **2023**, *16*, 2897. [CrossRef]
5. Yuan, J.; Xiao, Y.; Min, N.; Li, W.; Zhao, S. The influence of precipitate morphology on the growth of austenite grain in Nb-Ti-Al microalloyed steels. *Materials* **2022**, *15*, 3176. [CrossRef]
6. Zhao, Y.; Zheng, J.; Chen, L.; Liu, X. Static recrystallization behavior of low-carbon Nb-V-microalloyed forging steel. *Metals* **2022**, *12*, 1745. [CrossRef]
7. Zhang, Q.; Huo, X.; Li, L.; Chen, S.; Lu, C. Correlation between precipitation and recrystallisation during stress relaxation in titanium microalloyed steel. *Metals* **2022**, *12*, 1920. [CrossRef]
8. Kaikkonen, P.M.; Somani, M.C.; Karjalainen, L.P.; Kömi, J.I. Flow stress behaviour and static recrystallization characteristics of hot deformed austenite in microalloyed medium-carbon bainitic steels. *Metals* **2021**, *11*, 138. [CrossRef]
9. Felker, C.A.; Speer, J.G.; de Moor, E.; Findley, K.O. Hot strip mill processing simulations on a Ti-Mo microalloyed steel using hot torsion testing. *Metals* **2020**, *10*, 334. [CrossRef]
10. Buken, H.; Kozeschnik, E. Modeling static recrystallization in Al-Mg alloys. *Metall. Mater. Trans. A* **2021**, *52*, 544–552. [CrossRef]
11. Kozeschnik, E. Mean-field microstructure kinetics modeling. *Encycl. Mater. Met. Alloy.* **2022**, *4*, 521–526. [CrossRef]
12. CDL-IPE, Inst. of Mat. Sci. and Technol., TU Wien. Thermodynamic Database with Modified Carbo-Nitride Descriptions Based on the Open-License Multi-Component MatCalc Database mc_fe, Version 2.060. Available online: https://www.matcalc.at/images/stories/Download/Database/mc_fe_v2.060.tdb (accessed on 4 April 2023).

13. Varela-Castro, G.; Cabrera, J.-M.; Prado, J.-M. Critical Strain for Dynamic Recrystallisation. The Particular Case of Steels. *Metals* **2020**, *10*, 135. [CrossRef]
14. Uranga, P.; Fernández, A.; López, B.; Rodriguez-Ibabe, J. Transition between static and metadynamic recrystallization kinetics in coarse Nb microalloyed austenite. *Mater. Sci. Eng., A* **2003**, *345*, 319–327. [CrossRef]
15. Medina, S.F.; Gómez, M.; Rodríguez, E.; Rancel, L. Influence of accumulated stress in austenite on transformed ferrite grain size by hot rolling for a V-microalloyed steel. *ISIJ Int.* **2008**, *48*, 1263–1269. [CrossRef]
16. Vervynckt, S.; Verbeken, K.; Lopez, B.; Jonas, J.J. Modern HSLA steels and role of non-recrystallisation temperature. *Int. Mater. Rev.* **2012**, *57*, 187–207. [CrossRef]
17. Bai, D.Q.; Yue, S.; Sun, W.P.; Jonas, J.J. Effect of deformation parameters on the. *Met. Trans. A* **1993**, *24*, 2151–2159. [CrossRef]
18. Medina, S.F. Determination of no-recrystallisation temperature in Nb-V-Ti microalloyed steel and discussion of its definition. *Mater. Sci. Technol.* **1998**, *14*, 217–221. [CrossRef]
19. Gómez, M.; Medina, S.F.; Quispe, A.; Valles, P. Static recrystallization and induced precipitation in a low Nb microalloyed steel. *ISIJ Int.* **2002**, *42*, 423–431. [CrossRef]
20. Abad, R.; AI, F.; Lopez, B.; JM, R.-I. Interaction between recrystallization and precipitation during multipass rolling in a low carbon niobium microalloyed steel. *ISIJ Int.* **2001**, *41*, 1373–1382. [CrossRef]
21. Vervynckt, S.; Verbeken, K.; Thibaux, P.; Liebeherr, M.; Houbaert, Y. Austenite recrystallization–precipitation interaction in niobium microalloyed steels. *ISIJ Int.* **2009**, *49*, 911–920. [CrossRef]
22. Gómez, M.; Medina, S.F. Role of microalloying elements in the microstructure of hot rolled steels. *Int. J. Mater. Res.* **2011**, *102*, 1197–1207. [CrossRef]
23. Medina, S.F.; Mancilla, J.E.; Hernandez, C.A. Static recrystallization of hot deformed austenite and induced precipitation kinetics in vanadium microalloyed steels. *ISIJ Int.* **1994**, *34*, 689–696. [CrossRef]
24. Bhargava, G. Grain boundary effects on mechanical properties: Design approaches in steel. In *Welding—Modern Topics*; Crisóstomo Absi Alfaro, S., Borek, W., Tomiczek, B., Eds.; IntechOpen: London, UK, 2021; pp. 221–234. ISBN 978-1-83881-895-1.
25. Homsher, C.N. Determination of the Non-Recrystallization Temperature (Tnr) in Multiple Microalloyed Steels. Master's Thesis, Colorado School of Mines, Golden, CO, USA, 2013.
26. Akben, M.G.; Weiss, I.; Jonas, J.J. Dynamic precipitation and solute hardening in a V microalloyed steel and two Nb steels containing high levels of Mn. *Acta Metall.* **1981**, *29*, 111–121. [CrossRef]
27. Homsher-Ritosa, C.N. Influence of Processing Parameters and Alloying Additions on the mechanically Determined No-Recrystallization Temperature in Niobium Microalloyed Steels. Ph.D. Thesis, Colorado School of Mines, Golden, CO, USA, 2016.
28. Boratto, F.; Barbosa, R.; Yue, S.; Jonas, J.J. In Proceedings of the International Conference on Physical Metallurgy of Thermomechanical Processing of Steels and Other Metals, THERMEC-88, Tokyo, Japan, 6–10 June 1988. p. 383. Available online: https://www.worldcat.org/title/thermec-88-international-conference-on-physical-metallurgy-of-thermomechanical-processing-of-steels-and-other-metals-proceedings-june-6-10-1988-keidanren-kaikan-tokyo-japan/oclc/35486134 (accessed on 10 April 2023).
29. Maccagno, T.M.; Jonas, J.J.; Yue, S.; McCrady, J.; Slobodian, R.; Deeks, D. Determination of recrystallization stop temperature from rolling mill logs and comparison with laboratory simulation results. *ISIJ Int.* **1994**, *34*, 917–922. [CrossRef]
30. Bai, D.Q.; Bodnar, R.L.; Ward, J.; Dorricott, J.; Sanders, S. Development of discrete X80 line pipe plate at SSAB Americas. *Int. Symp. Recent Dev. Plate Steels* **2011**, *1*, 13–22.
31. Fletcher, F. Meta-analysis of Tnr measurements: Determining new empirical models based on composition and strain. In Proceedings of the Austenite Processing Symposium (Internal Company Presentation), Padua, Italy, 12 September 2008; pp. 1–14.
32. Medina, S.F.; Mancilla, J.E. Static recrystallization of austenite and strain induced precipitation kinetics in titanium microalloyed steels. *Acta Metall. Mater.* **1994**, *42*, 3945–3951. [CrossRef]
33. Medina, S.F.; Quispe, A. Influence of strain on induced precipitation kinetics in microalloyed steels. *ISIJ Int.* **1996**, *36*, 1295–1300. [CrossRef]
34. Medina, S.F.; Mancilla, J.E. Determination of static recrystallization critical temperature of austenite in microalloyed steels. *ISIJ Int.* **1993**, *33*, 1257–1264. [CrossRef]
35. Medina, S.F.; Quispe, A.; Valles, P.; JL, B. Recrystallization-precipitation interaction study of two medium carbon niobium microalloyed steels. *ISIJ Int.* **1999**, *39*, 913–922. [CrossRef]
36. Sobotka, E.; Kreyca, J.; Poletti, M.C.; Povoden-Karadeniz, E. Analysis and Modeling of Stress-strain Curves in Microalloyed Steels Based on a Dislocation Density Evolution Model. *Materials* **2022**, *15*, 6824. [CrossRef]
37. Facusseh, C.; Salinas, A.; Flores, A.; Altamirano, G. Study of static recrystallization kinetics and the evolution of austenite grain size by dynamic recrystallization refinement of an eutectoid steel. *Metals* **2019**, *9*, 1289. [CrossRef]
38. Perttula, J.S.; Karjalainen, L.P. Recrystallisation rates in austenite measured by double compression and stress relaxation methods. *Mater. Sci. Technol.* **1998**, *14*, 626–630. [CrossRef]
39. Palmiere, E.J.; Garcia, C.I.; DeArdo, A.J. The influence of niobium supersaturation in austenite on the static recrystallization behavior of low carbon microalloyed steels. *Metall. Mater. Trans. A* **1996**, *27*, 951–960. [CrossRef]
40. Khoddam, S.; Hodgson, P.D. Conversion of the hot torsion test results into flow curve with multiple regimes of hardening. *J. Mater. Process. Technol.* **2004**, *153–154*, 839–845. [CrossRef]

41. Ballard, T.J.; Speer, J.G.; Findley, K.O.; de Moor, E. Double twist torsion testing to determine the non recrystallization temperature. *Sci. Rep.* **2021**, *11*, 1–19. [CrossRef]
42. Rešković, S.; Slokar Benić, L.; Lovrenić-Jugović, M. The interdependence of the degree of precipitation and dislocation density during the thermomechanical treatment of microalloyed niobium steel. *Metals* **2020**, *10*, 294. [CrossRef]
43. Kocks, U.F.; Mecking, H. Physics and phenomenology of strain hardening: The FCC case. *Prog. Mater. Sci.* **2003**, *48*, 171–273. [CrossRef]
44. Stechauner, G.; Kozeschnik, E. Assessment of substitutional self-diffusion along short-circuit paths in Al, Fe and Ni. *Calphad* **2014**, *47*, 92–99. [CrossRef]
45. Sherstnev, P.; Lang, P.; Kozeschnik, E. Treatment of simultaneous deformation and solid-state precipitation in thermo-kinetic calculations: (ECCOMAS 2012). In Proceedings of the 6th European Congress on Computational Methods in Applied Sciences and Engineering (ECCOMAS 2012), Vienna, Austria, 10–14 September 2012; pp. 5331–5338.
46. Manohar, P.A.; Ferry, M.; Chandra, T. Five Decades of the Zener Equation. *ISIJ Int.* **1998**, *38*, 913–924. [CrossRef]
47. Cahn, J.W. The impurity-drag effect in grain boundary motion. *Acta Metall.* **1962**, *10*, 789–798. [CrossRef]
48. Buken, H.; Zamberger, S.; Kozeschnik, E. A model for the influence of micro-alloying elements on static recrystallization of austenite. In *Proceedings of the 6th International Conference on Recrystallization and Grain Growth (ReX&GG 2016)*; Wiley-VCH: Weinheim, Germany, 2016; pp. 113–118.
49. Bailey, J.E.; Hirsch, P.B. The recrystallization process in some polycrystalline metals. *Proc. R. Soc. A* **1962**, *267*, 11–30. [CrossRef]
50. Rehman, M.K.; Zurob, H.S. A novel approach to model static recrystallization of austenite during hot rolling of Nb microalloyed steel. Part I: Precipitate-free case. *Metall. Mater. Trans. A* **2013**, *44*, 1862–1871. [CrossRef]
51. Zurob, H.S.; Hutchinson, C.R.; Bréchet, Y.; Purdy, G.R. Modeling recrystallization of microalloyed austenite: Effect of coupling recovery, precipitation and recrystallization. *Acta Mater.* **2002**, *50*, 3077–3094. [CrossRef]
52. Xing, J.; Zhu, G.; Wu, B.; Ding, H.; Pan, H. Effect of Ti Addition on the Precipitation Mechanism and Precipitate Size in Nb-Microalloyed Steels. *Metals* **2022**, *12*, 245. [CrossRef]
53. Tang, S.; Li, X.; Li, J.; Liu, Z.; Wang, G. Role of microalloying elements on recrystallization kinetics of cold-rolled high strength low alloy steels. *Metals* **2022**, *12*, 1741. [CrossRef]
54. Leguen, C. Prior Austenite Grain Size Controlled by Precipitates. Ph.D. Thesis, Université de Lyon, Lyon, France.

Disclaimer/Publisher's Note: The statements, opinions and data contained in all publications are solely those of the individual author(s) and contributor(s) and not of MDPI and/or the editor(s). MDPI and/or the editor(s) disclaim responsibility for any injury to people or property resulting from any ideas, methods, instructions or products referred to in the content.